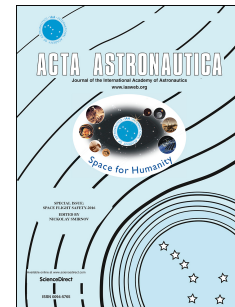


# Accepted Manuscript

Multi-fidelity orbit uncertainty propagation

Brandon A. Jones, Ryan Weisman



PII: S0094-5765(18)30480-6

DOI: [10.1016/j.actaastro.2018.10.023](https://doi.org/10.1016/j.actaastro.2018.10.023)

Reference: AA 7144

To appear in: *Acta Astronautica*

Received Date: 1 May 2018

Revised Date: 6 August 2018

Accepted Date: 13 October 2018

Please cite this article as: B.A. Jones, R. Weisman, Multi-fidelity orbit uncertainty propagation, *Acta Astronautica* (2018), doi: <https://doi.org/10.1016/j.actaastro.2018.10.023>.

This is a PDF file of an unedited manuscript that has been accepted for publication. As a service to our customers we are providing this early version of the manuscript. The manuscript will undergo copyediting, typesetting, and review of the resulting proof before it is published in its final form. Please note that during the production process errors may be discovered which could affect the content, and all legal disclaimers that apply to the journal pertain.

# Multi-Fidelity Orbit Uncertainty Propagation

Brandon A. Jones<sup>a,\*</sup>, Ryan Weisman<sup>b</sup>

<sup>a</sup>*Department of Aerospace Engineering and Engineering Mechanics,  
The University of Texas at Austin, C0600, Austin, Texas, United States of America*  
<sup>b</sup>*Space Vehicles Directorate, Air Force Research Laboratory, Albuquerque, New Mexico,  
United States of America*

## Abstract

To reduce computation time while limiting loss in accuracy when propagating an orbit state probability density function, this work seeks to develop an adaptive approach to multi-fidelity uncertainty propagation for applications in astrodynamics. Using the method of stochastic collocation, a set of particles produced via a low-fidelity solver defines a basis used in the surrogate over the space of propagated states. This basis allows for identifying a subset of important samples that are re-propagated using a high-fidelity propagator, which defines a correction for the original basis. This approach reduces computation time for propagating a particle ensemble or a Gaussian mixture model via the unscented transform. This paper demonstrates the efficacy of this method for several Earth-orbit test cases, and provides a means for merging general and special perturbation theories to produce a posterior probability density function more statistically consistent with a precise estimated state.

*Keywords:* uncertainty propagation, multi-fidelity methods, stochastic collocation

## 1. Introduction

Space situational awareness (SSA) is the monitoring of man-made space objects in Earth orbit to inform spacecraft operator decisions. This requires the prediction of a space-object catalog to identify risks to existing missions,

\*Corresponding author.

Email address: [brandon.jones@utexas.edu](mailto:brandon.jones@utexas.edu) (Brandon A. Jones)

update the orbit state estimates for each object, and enable sensor tasking. This prediction requires the propagation of an orbit state Probability Density Function (PDF) for each object in the catalog. Prediction of the PDF requires two important elements: (i) a tractable PDF approximation, and (ii) selection of dynamics models employed to describe propagation. Several approximations of the PDF have been proposed in the literature, including the use of Gaussian mixtures [1, 2], Polynomial Chaos Expansions (PCEs) [3, 4, 5], state transition tensors (STT) [6, 7, 8], and differential algebra [9, 10]. Instead, this paper focuses on the accuracy of the prediction and proposes a combination of different fidelity force models to propagate the selected orbit state PDF representation.

Higher-fidelity force models require increased computational complexity for their evaluation, but not all orbit regimes require the same models. For example, computational complexity for the evaluation of the spherical harmonic gravity field increases quadratically as a function of degree, but the magnitude of the acceleration for each term decreases rapidly with radius. This motivates the development of adaptive methods that use the minimum degree expansion required at a given altitude for the sake of efficiency (e.g., see [11]). While research exists to leverage advances in computing hardware, e.g., interpolation-based models of the gravity field [12], the use of such implementations is not required over all orbit regimes.

In the context of astrodynamics, a spectrum of force models exist with limited research into their optimal combination for computationally efficient orbit state uncertainty propagation. The method of multiple scales allows for integrating slow time-scale effects and applying a known analytic correction for the fast time scale perturbations in a semi-analytic framework [13]. General Perturbation (GP) and Special Perturbation (SP) theories are usually considered mutually exclusive when propagating an orbit PDF. GP allows for rapid propagation of an orbit's state vector and accounts for the secular- and long-period variations in an orbit encompassing the largest contributions to orbital dynamics. SP offers a high-fidelity solution at the cost of increased computation time, and includes short-period variations and the contribution of any forces that cannot be modeled in a semi-analytic form. One motivation of this research is to leverage the speed of GP propagation with a data derived SP-based correction to the solution that achieves improved PDF consistency without the derivation of new theory. Combinations of GP and SP theory for orbit propagation are not unique to this work and have been demonstrated in other, single-state prediction research. Variable-fidelity models

have been used to reduce the computation time requirements for orbit state propagation using implicit Runge-Kutta integrators (e.g., see [14]). In such methods, a low-fidelity (sometimes semi-analytic) solution is used to provide a “warm start” for a nonlinear solution to the implicit integration equations, which enables longer integrator step sizes. This shares the motivation of multi-fidelity uncertainty quantification, i.e., the use of low-fidelity models to achieve an approximate solution and a reduced number of high-fidelity model evaluations to correct the initial solution.

Previous work in multi-fidelity uncertainty quantification may be found in the literature in both the uncertainty quantification and, to a limited extent, the astrodynamics community. The survey paper [15] provides a description of recently developed methods for uncertainty propagation, estimation, and optimization. In [16], the authors propose a method of multi-fidelity uncertainty quantification based on stochastic collocation. Such an approach combines low- and high-fidelity propagated samples to build a surrogate for the response surface for quantities of interest as a function of random variables. Conditions for and proofs of convergence may be found in [16], and [17] discusses the implementation and computational elements of the approach. In [18], the authors propose a related algorithm based on a low-rank approximation. In regards to propagating orbit-state uncertainty, [19] considered a weighted combination of PDF moments generated using low-fidelity samples propagated via GP theory and a state transition tensor to reduce computational complexity. That work studied the sensitivities of the weighted combination of moments as a function of the initial state PDF, but ignored variations in the force model fidelities.

This paper presents the application of the stochastic collocation approach to multi-fidelity uncertainty propagation presented in [16, 17] to a set of astrodynamics problems. The multi-fidelity approach yields a reduced computation time when compared to both a Monte Carlo analysis and propagation of the orbit-state PDF via a Gaussian Mixture (GM) model with the unscented transform. In the case of the GM representation of the PDF, the multi-fidelity approach allows for faster propagation of the sigma points in the unscented transform. Test cases include a duplication of those in [13] with a specified uncertainty. We then combine the multi-fidelity approach with propagation of a Gaussian-mixture model of the *a posteriori* PDF. We also present the use of the multi-fidelity approach to jointly propagate a Two-Line Element (TLE), with specified uncertainty, via general and special perturbation theory.

The paper is organized as follows. Section 2 describes the formulation of the multi-fidelity uncertainty propagation problem. Section 3 presents the approach employed in this work based on stochastic collocation and the associated customizations for the astrodynamics applications presented in this paper. Section 4 describes how the multi-fidelity approach is combined with a Gaussian mixture approximation of the state PDF to reduce computation time for its propagation. Section 5 presents simulations and results demonstrating the efficacy of the approach, followed by conclusions and an outline of future work.

## 2. Formulation of Governing Stochastic System

This section describes the general orbit-state uncertainty propagation problem. Let  $(\mathcal{S}, \Sigma, \mathcal{P})$  be a probability space with the sample space  $\mathcal{S}$ , probability measure  $\mathcal{P}$ , and  $\sigma$ -algebra  $\Sigma$ . The random input vector  $\boldsymbol{\xi} \in \mathbb{R}^d : \mathcal{S} \rightarrow \Gamma^d \subseteq \mathbb{R}^d$  defined on  $(\mathcal{S}, \Sigma, \mathcal{P})$  includes the  $d$  independent random inputs characterizing the stochastic system. The space  $\Gamma^d$  depends on the problem. For example,  $\Gamma^d = [0, 1]^d$  for  $d$ -dimensional uniform random variables in the range  $[0, 1]$ . The uncertainty propagation problem seeks to generate a solution to the stochastic ordinary differential equations

$$\mathcal{A}(t, \boldsymbol{\xi}; \mathbf{x}) = 0, \quad (t, \boldsymbol{\xi}) \in [0, t_f] \times \Gamma^d, \quad \mathcal{P} - \text{a.s. in } \mathcal{S} \quad (1)$$

where  $t \in [0, t_f]$  is the time variable,  $\mathbf{x} \in \mathbb{R}^n$  is a vector of Quantities of Interest (QoIs), and  $\mathcal{A}$  is the stochastic ODE operator that defines the flow of  $\mathbf{x}$  to  $t$  as a function of  $\boldsymbol{\xi}$ . Hence, a solution to the uncertainty propagation problem quantifies the effects of random inputs  $\boldsymbol{\xi}$  on the random QoIs  $\mathbf{x}$ . In an ideal setting, the highest fidelity dynamic models define the propagation operator  $\mathcal{A}$ . However, this work considers the case of employing lower-fidelity models to generate an approximation to  $\mathcal{A}$  with sufficient accuracy.

In the context of orbit uncertainty propagation, often

$$\mathbf{x}(\boldsymbol{\xi}) = \begin{bmatrix} \mathbf{r}(t, \boldsymbol{\xi}) \\ \dot{\mathbf{r}}(t, \boldsymbol{\xi}) \end{bmatrix}, \quad (2)$$

where  $\mathbf{r}$  is the position vector. When desired,  $\mathbf{x}$  may instead be a prescribed orbit element set or any other QoIs. Note that dependence on time is omitted from  $\mathbf{x}$  since individual elements may be at different times.

To illustrate the dependence of  $\mathbf{x}(\xi)$  on  $\xi$ , consider the case where  $\xi \in \mathbb{R}^6$  and known *a priori* state PDF

$$\begin{bmatrix} \mathbf{r}(0) \\ \dot{\mathbf{r}}(0) \end{bmatrix} \sim \mathcal{N} \left( \begin{bmatrix} \bar{\mathbf{r}}_0 \\ \dot{\bar{\mathbf{r}}}_0 \end{bmatrix}, \mathbf{P}_0 \right), \quad (3)$$

where  $\mathbf{P} \in \mathbb{R}^{6 \times 6}$  is the covariance matrix for the state,  $\bar{\mathbf{r}}$  and  $\dot{\bar{\mathbf{r}}}$  indicate the mean position and velocity, respectively, and the  $*_0$  subscript indicates at  $t = 0$ . This prior PDF is typically generated using an orbit determination algorithm. Monte Carlo samples are then generated via

$$\begin{bmatrix} \mathbf{r}(0, \xi) \\ \dot{\mathbf{r}}(0, \xi) \end{bmatrix} = \begin{bmatrix} \bar{\mathbf{r}}_0 \\ \dot{\bar{\mathbf{r}}}_0 \end{bmatrix} + \mathbf{S}\xi, \quad (4)$$

where  $\xi \sim \mathcal{N}(\mathbf{0}, \mathbb{I}_6)$  are generated in numeric simulations using a pseudo-random number generator, and  $\mathbf{S}$  is the Cholesky decomposition such that  $\mathbf{P}_0 = \mathbf{S}\mathbf{S}^T$ . Similar mappings may be used if any elements of  $\xi$  are, for example, uniformly distributed. The produced Monte Carlo sample may then be propagated to  $t$  to produce the example  $\mathbf{x}(\xi)$  in (2).

### 3. Multi-Fidelity Orbit Propagation of Samples

This section describes an approach for multi-fidelity propagation of a particle ensemble using stochastic collocation with application to orbit propagation models of variable fidelity. The fidelity of the propagation refers to: (i) the theory involved to produce the propagated orbit (general perturbation versus special perturbation propagation theory), and/or (ii) the accuracy and truncation of force models included in a given propagator. The multi-fidelity uncertainty propagation method employed here assumes that reduced-fidelity methods provide an adequate basis for the space of propagated samples. This basis is then corrected using a sub-set of higher-fidelity propagated samples to provide a correction for the basis. This approach shares similarities with minimum system identification realization approaches such as the eigensystem realization algorithm (e.g., see [20]). While not employed here, [21] describes an approach for characterizing performance (e.g., if the low-fidelity model satisfies accuracy requirements) for an increased computation cost.

#### 3.1. Multi-Fidelity Solution via Stochastic Collocation

Methods based on stochastic collocation readily provide a framework for multi-fidelity uncertainty quantification [16, 17]. This approach employs a

set of low-fidelity samples  $\mathbf{x}^L(\boldsymbol{\xi})$  and identifies a subset to propagate using a high-fidelity model. Let  $\mathbf{x}^H(\boldsymbol{\xi})$  be the QoI vector using a high-fidelity propagator. Given a set of random inputs  $\Xi = \{\boldsymbol{\xi}_i\}_{i=1}^m$ , then

$$\mathbf{X}^H(\Xi) \equiv [\mathbf{x}^H(\boldsymbol{\xi}_1) \ \cdots \ \mathbf{x}^H(\boldsymbol{\xi}_m)] \in \mathbb{R}^{n \times m}, \quad (5)$$

$$\mathbb{X}^H(\Xi) \equiv \text{span}(\mathbf{X}^H(\Xi)) = \text{span}[\mathbf{x}^H(\boldsymbol{\xi}_1) \ \cdots \ \mathbf{x}^H(\boldsymbol{\xi}_m)], \quad (6)$$

with a similar definition for  $\mathbf{X}^L(\Xi)$  and  $\mathbb{X}^L(\Xi)$ . For the sake of a simplified notation, we drop dependence on  $\Xi$  except where the input set is not clear. We seek a stochastic collocation surrogate

$$\mathbf{x}^H(\boldsymbol{\xi}) \approx \hat{\mathbf{x}}^H(\boldsymbol{\xi}) = \sum_{\ell=1}^r c_\ell(\boldsymbol{\xi}) \mathbf{x}^H(\bar{\boldsymbol{\xi}}_\ell), \quad (7)$$

where the  $\hat{\cdot}$  denotes an approximate value of the variable  $*$ ,  $c_\ell$  are expansion coefficients,  $\bar{\boldsymbol{\xi}}_\ell$  are the random inputs for the collocation points in the expansion, and  $r$  is dubbed the *rank* of the surrogate with  $r \ll m$ . The discussion below presents how to solve for  $c_\ell$ ,  $\bar{\boldsymbol{\xi}}_\ell$ , and  $r$ .

The multi-fidelity approach employed here requires two assumptions common in similar methods (e.g., see [18]). We first assume that  $\mathbf{X}^L \in \mathbb{R}^{n \times m}$ ,  $r \leq n \ll m$  allows for the identification of sample points  $\bar{\boldsymbol{\xi}}_\ell$  to produce a sufficiently accurate basis for  $\mathbf{x}^H(\boldsymbol{\xi})$ . Second, the coefficients  $c_\ell$  in

$$\mathbf{x}^L(\boldsymbol{\xi}) \approx \hat{\mathbf{x}}^L(\boldsymbol{\xi}) = \sum_{\ell=1}^r c_\ell(\boldsymbol{\xi}) \mathbf{x}^L(\bar{\boldsymbol{\xi}}_\ell) \quad (8)$$

may be identically applied in (7) using high-fidelity realizations  $\mathbf{x}^H(\bar{\boldsymbol{\xi}}_\ell)$  with sufficient accuracy. Let

$$\bar{\Xi} \equiv \{\bar{\boldsymbol{\xi}}_\ell\}_{\ell=1}^r \quad (9)$$

denote a set of random inputs dubbed the “important” samples required to generate  $\mathbf{x}^H(\bar{\boldsymbol{\xi}}_\ell)$ . In this approach, we use  $\mathbf{X}^L$  to select the  $r$  important samples to use in the high-fidelity propagator. Note that this process differs from the method of importance sampling employed in Monte Carlo uncertainty quantification.

Let  $\Xi^{k-1} = \{\bar{\boldsymbol{\xi}}_1, \dots, \bar{\boldsymbol{\xi}}_{k-1}\}$  for  $k > 1$  be the current set of  $k-1$  important random samples. Note, for  $k=1$ ,  $\Xi^0 = \{\}$ . The  $k$ th sample is then found by solving the problem

$$\bar{\boldsymbol{\xi}}_k = \arg \max_{\boldsymbol{\xi} \in \Xi} \text{dist}(\mathbf{x}^L(\boldsymbol{\xi}), \mathbb{X}^L(\Xi^{k-1})), \quad (10)$$

where

$$\text{dist}(\mathbf{x}, \mathbb{X}) \equiv \inf_{\mathbf{y} \in \mathbb{X}} \|\mathbf{x} - \mathbf{y}\|, \quad (11)$$

and

$$\Xi^k = \Xi^{k-1} \cup \{\bar{\xi}_k\}. \quad (12)$$

Conceptually,  $\text{dist}()$  is a distance between the point  $\mathbf{x}$  and the space  $\mathbb{X}$ . By iteratively solving the optimization problem in (10), we build the set  $\bar{\Xi} = \Xi^k$  via (12) until  $k = r + 1$ . This greedy algorithm builds a space with basis vectors  $\mathbf{x}^L(\bar{\xi}_\ell)$ ,  $\ell = 1, \dots, r$  that minimize the distance (11) between points in  $\mathbf{X}^L(\Xi)$  and the span  $\mathbb{X}^L(\bar{\Xi})$ .

In general, solving (10) is non-trivial, and we employ the approximate solution described in [17]. This approach generates  $\bar{\Xi}$  by solving the pivoted Cholesky decomposition

$$[\mathbf{X}^L]^T \mathbf{G}^L [\mathbf{X}^L] = \mathbf{A}^T \mathbf{L} \mathbf{L}^T \mathbf{A} \quad (13)$$

with brackets introduced to differentiate between the  $L$  and  $T$  superscripts,  $\mathbf{G}^L$  is the Gramian matrix of the low-fidelity samples, and  $\mathbf{A}$  is a pivot matrix that orders samples based on the optimization problem posed in (10). Algorithm 1 of [17] details how to generate  $\mathbf{L}$  and  $\bar{\Xi}$  without computing the full Cholesky decomposition, which is duplicated in the Appendix for reference. Note that the algorithm produces the full set  $\bar{\Xi}$  and removes the need for iteration (i.e., building the set via (12)).

The coefficients  $c_\ell$  in (8) are generated via

$$\mathbf{L} \mathbf{L}^T \mathbf{c} = \mathbf{g}, \quad (14)$$

where

$$g_\ell = \langle \mathbf{x}^L(\xi), \mathbf{x}^L(\bar{\xi}_\ell) \rangle, \quad \ell = 1, \dots, r \quad (15)$$

the  $\langle \cdot, \cdot \rangle$  operator is the (discrete) inner product, and  $\mathbf{L}$  is lower-triangular and produced in the selection of  $\bar{\Xi}$ . We use forward/backward substitution to solve for the elements  $c_\ell$  of  $\mathbf{c}$ , and then produce approximate high-fidelity samples using (7) and these values of  $c_\ell$ .

The previous discussion assumes a known value of  $r$ . In this work,  $r$  is selected such that

$$\left\| \mathbf{X}^L - \widehat{\mathbf{X}}^L \right\|_{\infty} < \varepsilon, \quad (16)$$

where

$$\widehat{\mathbf{X}}^L \equiv [\widehat{\mathbf{x}}^L(\xi_1) \ \cdots \ \widehat{\mathbf{x}}^L(\xi_m)], \quad (17)$$

$\varepsilon$  is a prescribed tolerance, and  $\|\cdot\|_{\infty}$  denotes the infinity norm. An initial value  $r = 1$  is selected, and the algorithm above (with  $\mathbf{X}^L$  fixed) is repeated for increasing  $r$  until the condition (16) is satisfied. The low-fidelity samples must only be propagated once. Unless stated otherwise for a given test case,  $\varepsilon = 1$  m.

Tri-fidelity uncertainty propagation employs a slight variation on the previous bi-fidelity procedure. Medium fidelity is defined as a model that produces samples  $\mathbf{x}^M(\xi)$  with a computation cost larger than the low-fidelity model, but small enough to be evaluated  $r$  times. The samples  $\mathbf{X}^L(\Xi)$  are used to get  $\Xi$ . Upon using the medium-fidelity model to get  $\mathbf{X}^M(\Xi)$ , then Algorithm 1 of [17] yields  $\mathbf{L}^M$ . Finally, (7) produces  $\widehat{\mathbf{x}}^H(\xi)$  using  $\mathbf{L}^M$  and  $\mathbf{x}^M(\xi_\ell)$  instead of the low-fidelity counter-parts. Said differently, the low-fidelity model is used to identify important samples, coefficients  $c_\ell$  are based on the medium fidelity model, and the final approximation uses high-fidelity collocation points  $\mathbf{x}^H(\Xi_\ell)$ .

### 3.2. Multi-Fidelity Orbit Uncertainty Propagation

The multi-fidelity methods discussed previously require  $n \geq r$  where  $\mathbf{x}(\xi) \in \mathbb{R}^n$ . In the case of orbit-state propagation,  $n$  usually equals 6, which puts an upper limit on the number of possible important samples identified for high-fidelity propagation. This limitation produces an expansion with insufficient accuracy (see Section 5.1.1). Instead, this work increases  $n$  by considering the state trajectory, i.e.,

$$\mathbf{x}(\xi) = \begin{bmatrix} \mathbf{r}(t_1, \xi) \\ \dot{\mathbf{r}}(t_1, \xi) \\ \mathbf{r}(t_2, \xi) \\ \dot{\mathbf{r}}(t_2, \xi) \\ \vdots \\ \mathbf{r}(t_T, \xi) \\ \dot{\mathbf{r}}(t_T, \xi) \end{bmatrix} \quad (18)$$

where  $t_{i+1} = t_i + \delta t$ ,  $i = 1, \dots, T$ , and  $T$  is a sufficiently large number of time instances. For a given  $\xi$ , this definition of  $\mathbf{x}(\xi)$  includes the position and velocity state for a single trajectory at different points in time  $t_i$ . This produces a QoI vector of sufficient length to generate  $r < n$  and a high-fidelity surrogate of sufficient accuracy.

Increasing the length of the state vector is not without justification. In the context of SSA, many analyses require the propagated PDF over a given time interval. For example, sensor tasking requires knowledge of the state PDF over a period of time to identify access times and generate an observation schedule (e.g., see [22]). As demonstrated in the following numeric simulations, the computation cost of the surrogate with the penalty to propagate up to  $T$  points in time still yields a net computation savings to justify the approach.

#### 4. Multi-Fidelity Propagation of Gaussian Mixture Models

Gaussian Mixture (GM) models provide a means for approximating an arbitrary PDF via a weighted sum of Gaussian components, i.e.,

$$p(\mathbf{x}) = \sum_{j=1}^J w_j p_N(\mathbf{x}; \mathbf{m}_j, \mathbf{P}_j), \quad (19)$$

where  $w_j \geq 0$ ,  $\sum w_j = 1$ ,  $p_N$  denotes the multi-dimensional Gaussian distribution, and  $\mathbf{m}_j$  and  $\mathbf{P}_j$  are the mean and covariance, respectively, of the  $j$ th component. Note that  $\mathbf{P}_j = \mathbf{S}_j \mathbf{S}_j^T$ . Each component may be propagated using a prescribed method such as the first-order linearization method (e.g., see [23]) or the higher-order unscented transform [24]. The unscented transform propagates a collection of points  $\mathbf{x}^{(i)}$  forward in time, and generates the propagated Gaussian PDF via a weighted sum of propagated sigma points and their deviation from the mean. This work uses the square-root unscented transform presented in [25] with  $\alpha = 1$  and  $\beta = 2$ , which requires  $2n + 1$  points per GM component. A key advantage of employing the mixture in (19) is the use of a GM filter to fuse new knowledge gained through measurements [26, 27].

The multi-fidelity approach employed here reduces the computation time required to propagate the GM model by using the stochastic collocation approach for propagating the sigma points. This section first describes the multi-fidelity approach to propagating the GM, and a second method that

employs autonomous splitting of the GM over time based on the dynamics model. This latter method serves as a baseline for comparison in the future numeric results section.

#### 4.1. Splitting a GM Component

Approximating a single GM component as a mixture requires splitting a single component into multiple ones. DeMars et al. [1] provide three- and five-component splitting libraries, and Horwood and Poore [2] propose a splitting method based on Gauss-Hermite quadrature weights and nodes. The method proposed in [28] allows for splitting a single component along multiple arbitrary directions using up to 39 sub-components in a single direction. Let  $\hat{\mathbf{a}}$  be the desired direction of the split operation for a component with weight  $w$ , mean vector  $\mathbf{m}$ , and covariance  $\mathbf{P}$ . Given a  $K$ -component splitting library in a single direction with weight  $\alpha_k$ , mean  $m_k$ , and variance  $\sigma^2$ , then [28]

$$w_k = \alpha_k w, \quad (20)$$

$$\mathbf{m}_k = \mathbf{m} + m_k \mathbf{S} \hat{\mathbf{a}}^*, \quad (21)$$

$$\mathbf{P}_k = \mathbf{S} (\mathbb{I}_n + (\sigma^2 - 1) \hat{\mathbf{a}}^* \hat{\mathbf{a}}^{*T}) \mathbf{S}^T, \quad (22)$$

$$\hat{\mathbf{a}}^* = \mathbf{S}^{-1} \hat{\mathbf{a}} / \|\mathbf{S}^{-1} \hat{\mathbf{a}}\|_2. \quad (23)$$

Note that  $\sigma^2$  is the same for all  $j$ , and  $\hat{\mathbf{a}}^*$  is a unit vector in the square-root frame of  $\mathbf{P}$  with transformation  $\mathbf{S}$  (for further details, see [28]).

The algorithm outlined previously enables splitting in a single direction. Splitting along multiple directions  $\hat{\mathbf{a}}_1, \dots, \hat{\mathbf{a}}_I$  requires repeated application of the splitting operations in each direction, i.e., splitting in the  $\hat{\mathbf{a}}_1$  direction, then splitting all resulting components in the  $\hat{\mathbf{a}}_2$  direction, etc. For a  $K$ -component library and  $I$  directions, this yields  $K^I$  components. Figure 1 illustrates the splitting along two directions with the radius of the ellipse for each component scaled by its weight to depict relative contributions to the GM model.

#### 4.2. Selecting the Splitting Direction

Component splitting requires the selection of a direction, or directions, based on a specified criterion. Development of an optimal adaptive algorithm (in the sense of minimum computation cost) is outside of the scope of this paper, and this work employs an existing method to demonstrate the

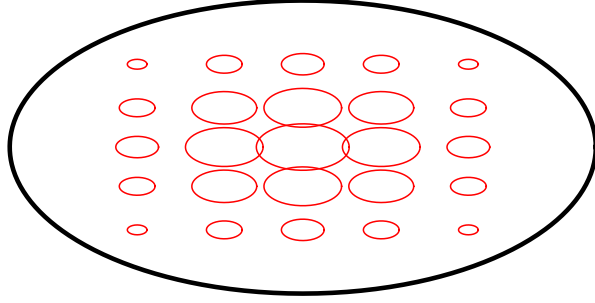


Figure 1: Bi-variate Gaussian distribution (ellipse with thicker line) split into five components in each direction.

applicability of multi-fidelity propagation for a GM. Let the term “eigendirection” refer to the direction in  $n$ -dimensional space corresponding to a given eigenvector of the covariance matrix  $\mathbf{P}_j$ . The approach in [1] splits a GM component along the eigendirection with the largest eigenvalue, and [2] generalizes this to a subset of eigendirections with the largest eigenvalues. Both of these methods assume a direct correlation between sensitivity of the predicted PDF at time  $t_f$  and eigendirections with the largest eigenvalues at  $t_0$ .

Instead, [28] proposes ranking splitting directions (e.g., the eigendirections) based on a measure of sensitivity of the PDF at  $t_f$  to the directions at  $t_0$ . Let  $\hat{\mathbf{a}}$  be a unit vector for an arbitrary direction at  $t_0$  and  $f(\mathbf{m})$  the propagated state vector  $\mathbf{m}$  to time  $t_f$ , then

$$NL_j(\hat{\mathbf{a}}) = \frac{f(\mathbf{m}_j + \tilde{h}\sigma_{\hat{\mathbf{a}}}\hat{\mathbf{a}}) + f(\mathbf{m}_j - \tilde{h}\sigma_{\hat{\mathbf{a}}}\hat{\mathbf{a}}) - 2f(\mathbf{m}_j)}{2\tilde{h}^2}, \quad (24)$$

provides a measure of nonlinearity (after propagation) in the  $\hat{\mathbf{a}}$  direction where

$$\sigma_{\hat{\mathbf{a}}} = \|\mathbf{S}_j^{-1}\hat{\mathbf{a}}\|_2^{-1}. \quad (25)$$

Using  $\tilde{h} = \sqrt{3}$  produces the sigma points employed in the unscented transformation if  $\hat{\mathbf{a}}$  is based on columns of  $\mathbf{S}_j$  [28]. This work ranks the  $n$  eigendirections via this nonlinearity measure, and Section 5.1.2 presents results with variations in the number of splitting directions.

#### 4.3. Multi-Fidelity Propagation of Sigma Points

Upon splitting a GM component at time  $t_0$  for propagation to  $t_f$ , the multi-fidelity approach for stochastic collocation reduces the computation time required for propagating the GM model. For the sake of generality, assume that (19) is the PDF at  $t_0$ . Let  $\phi$  be a discrete random variable over the set  $\{1, \dots, J\}$  with probability mass function  $\mathcal{P}(j) = w_j$ , and  $\boldsymbol{\theta} \sim \mathcal{N}(\mathbf{0}, \mathbb{I}_n)$ . Random inputs for the GM may then be defined as the  $d$ -dimensional vector  $\boldsymbol{\xi} = [\phi, \boldsymbol{\theta}^T]^T$ , where  $d = n + 1$ ,  $\phi$  determines the component, and  $\boldsymbol{\theta}$  defines the random sample of that component.

While the unscented transform deterministically generates the set of sigma points to propagate, the multi-fidelity approach requires the input set of random inputs  $\Xi$  corresponding to the points at  $t_0$ . Let  $\boldsymbol{\zeta}_j^{(i)}(t_0)$  be the  $i$ th sigma point for the  $j$ th component. The random input  $\boldsymbol{\xi}_{i,j} = [\phi_{i,j}, \boldsymbol{\theta}_{i,j}^T]^T$ , associated with each point may be found via

$$\phi_{i,j} = j \quad (26)$$

$$\boldsymbol{\theta}_{i,j} = \mathbf{S}_j^{-1} \left( \boldsymbol{\zeta}_j^{(i)}(t_0) - \mathbf{m}_j \right). \quad (27)$$

Hence, given the  $J \cdot (2n + 1)$  sigma points,

$$\Xi = \{\boldsymbol{\xi}_{i,j}\}, \quad i = 1, \dots, 2n + 1, \quad j = 1, \dots, J. \quad (28)$$

The multi-fidelity stochastic collocation method described in Section 3.1 yields an approximate solution to  $\boldsymbol{\zeta}_j^{(i)}(t_f)$  for each sigma point. As demonstrated in the numeric results section, this reduces the computational burden in propagating the GM model.

#### 4.4. Summary of Multi-Fidelity Propagation of Gaussian Mixture

In summary, the approach for multi-fidelity propagation of a single Gaussian component of a PDF may be summarized by:

1. Compute the eigenvector/value decomposition of the covariance matrix  $\mathbf{P}_j$ .
2. For each of the eigendirections, evaluate (24) using the low-fidelity propagator.
3. Using the approach in Section 4.1, split the GM component along the  $D$  eigendirections with the largest sensitivities  $NL(\hat{\mathbf{a}})$ .

4. Generate the sigma points for each of the  $J$  components, and use the procedure in Section 4.3 to get  $\Xi(\xi_{i,j})$ .
5. Propagate the sigma points using the multi-fidelity stochastic collocation approach in Section 3.1.
6. Use the propagated sigma points to compute the propagated mean and covariance for each component via the unscented transform.

As demonstrated in Section 5.1.2, this approach reduces the computation time for propagating a GM model via the unscented transform. Step 2 assumes that the low-fidelity propagator yields sufficient accuracy in  $NL(\hat{\mathbf{a}})$  to rank the eigendirections. This is consistent with the requirement that low-fidelity samples yield an adequate basis for multi-fidelity stochastic collocation. In this work,  $D$  is a design parameter, and numeric tests consider variations in its value and its effect on performance. While the previous description of the approach assumes a single Gaussian component at epoch, generalization to multiple initial components is straightforward and not included for brevity.

## 5. Numeric Simulations

This section presents application of the multi-fidelity approach to uncertainty propagation for several test cases. The first section presents results for three cases: (i) two low-Earth orbiter scenarios, and (ii) a highly elliptic (Molniya) orbit. This includes characterizing the accuracy and runtime required for generating the corrected surrogate  $\hat{\mathbf{x}}^H(\xi)$  and its use for propagating a GM model. The subsequent section briefly demonstrates improved understanding of the orbit-state uncertainty when using a TLE for the initial state knowledge and augmenting the propagation of uncertainty with a high-fidelity model. For all cases, errors in the surrogate are based on an independent set of samples  $\Xi'$ , which better describes the accuracy of the approximation. All cases use  $\delta t = 30$  sec and  $T = 20$  instances with results presented at  $t_1$  for comparison. Runtime tests are generated via a single processor (parallelization disabled except as stated for the GM propagation case) on a MacBook Pro running macOS 10.12.5 with a 2.8 GHz Intel Core i7 processor and 16 GB of random-access memory. The propagation software is written in C/C++ and compiled with the Clang 8.0 compiler. Generation of the surrogate leverages software written in Python with linear algebra operations realized using the NumPy and SciPy modules.

*Table 1: Orbit state initial conditions and  $1\sigma$  uncertainty*

	$a$ [km]	$e$	$i$ [deg]	$\Omega$ [deg]	$\omega$ [deg]	$\nu$ [deg]
Test Case 1	7078	0.01	30	0	0	0
Test Case 2	26562	0.74	63.4	0	0	0
Test Case 3	6878	$7.7 \times 10^{-4}$	45	0	90	0
$\sigma$	10.0	$10^{-3}$	1/36	1/36	1/36	1/36

*Table 2: Force models for low- and high-fidelity fully simulated tests*

Model	Low-Fidelity	High-Fidelity
Central Body Gravity	Two-Body and $J_2$	$70 \times 70$
Third-Body Perturbations	None	Sun and Moon
Solar Radiation Pressure	None	Cannonball
Atmospheric Drag	None	Cannonball
Coordinate System Reduction	None	IAU2006 [30]

### 5.1. Synthetic Scenarios

Tests in this section consider the propagation of uncertainty for orbits defined in Table 1 under the influence of forces in Table 2. The initial-state PDF defined in Table 1 is converted to Cartesian coordinates in the inertial frame using the unscented transform. Duration of the propagation varies slightly with each of the test cases, but is approximately one day. Atmospheric density is modeled using the 1978 standard exponential model. The JPL DE430 ephemerides [29] determines the locations of the third-bodies. Other inputs for the propagation may be found in Table 3. The coordinate system reduction model is not evaluated in the low-fidelity propagator since the dynamics model only includes the zonal  $J_2$  term. Hence, the low-fidelity model also includes dynamic model error associated with truncating polar motion, nutation, and precession in conversion between the Earth-fixed and inertial frames. All cases use 1,000 low-fidelity samples with the number of high-fidelity propagations based on the determined value of  $r$ .

#### 5.1.1. Stochastic Collocation Performance

This section characterizes performance of the multi-fidelity approach for propagating a particle ensemble. This includes demonstrating variations in

Table 3: Force model and satellite parameters for all cases

Parameter	Value
Satellite Mass	500 kg
Satellite Drag and SRP Area	1 m <sup>2</sup>
$C_D$	2.0
$C_R$	1.5
Epoch Time	2455200.5 UTC

accuracy and runtime based on different design parameters (e.g.,  $\varepsilon$ ). Results of this section determine the configuration used in the following section for propagating a GM approximation of the state PDF.

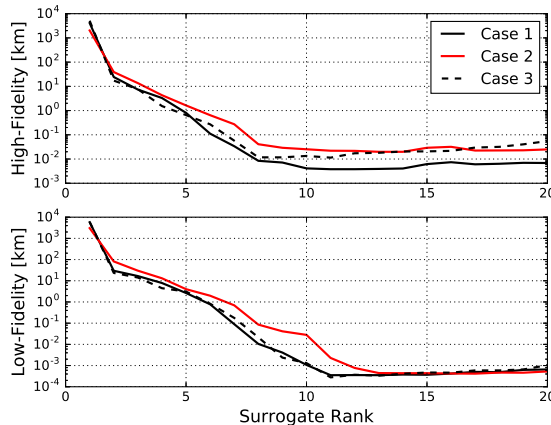
Figure 2: Accuracy for high-fidelity ( $\hat{\mathbf{x}}^H$ ) and low-fidelity ( $\hat{\mathbf{x}}^L$ ) surrogates.

Figure 2 demonstrates the convergence of the low- and high-fidelity expansions as a function of  $r$ . In this context, low-fidelity convergence refers to the achieved error defined in (16). High-fidelity surrogate accuracy is quantified by the position Root-Mean-Square (RMS) error when compared to  $10^5$  independently propagated samples. These tests indicate the  $\varepsilon = 1$  m used in generation of future surrogates is the smallest value possible for these test cases and with the two-body and  $J_2$  low-fidelity model. While details are provided below for the selected convergence criteria, high-fidelity RMS accuracy is on the order of meters to 10s of meters.

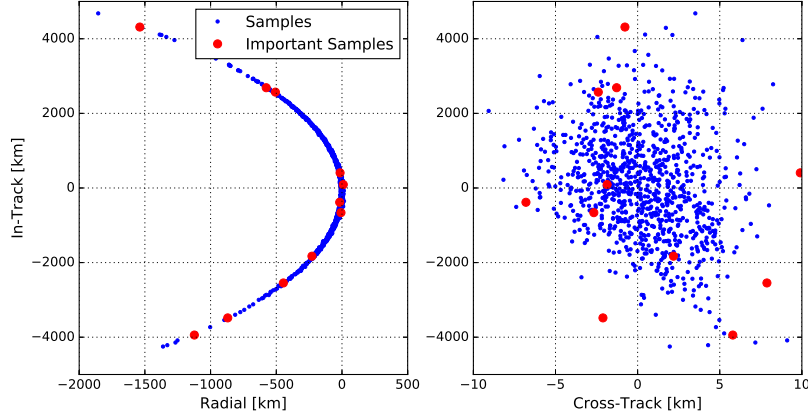


Figure 3: Scatter of propagated samples in the RIC frame of the propagated initial mean vector for test case 1.

Figure 3 illustrates the distribution of 1,000 randomly generated samples  $\mathbf{x}^H(\xi)$  propagated in time where  $t_1 = 24$  hours and rotated into the Radial, In-track, and Cross-track (RIC) frame. Presented results are at  $t_1$ . This RIC frame is defined by the propagated mean state defined by Table 1. In the Cartesian frame, the position PDF is non-Gaussian. Red/large dots denote the propagated collocation points  $\mathbf{x}^H(\bar{\xi}_\ell)$  and are provided for reference.

Figure 4 illustrates the effectiveness of correcting the propagated samples using  $r = 11$  propagated high-fidelity samples. The top image describes the distribution of the root-sum-square (RSS) errors of the position elements of  $\hat{\mathbf{x}}^H(\xi) - \mathbf{x}^H(\xi)$ , i.e., the error in the corrected sample position when compared to the true high-fidelity result. The lower image illustrates the error due to the force model truncation, i.e.,  $\mathbf{x}^L(\xi) - \mathbf{x}^H(\xi)$ . This demonstrates that the low-rank approximation produces a significant improvement in the propagated low-fidelity samples.

Figure 5 describes the propagated samples for the second case at  $t_1 \approx 0.992$  days. This places the propagated mean vector approximately at perigee at the time of interest. The posterior PDF is non-Gaussian, which is expected for this orbit. Fig. 6 demonstrates that the low-rank approximation with  $r = 12$  high-fidelity propagations achieves RSS position accuracy on the order of tens-of-meters at the time of interest. As discussed later, this case actually achieved the largest reduction in error when compared to that of the

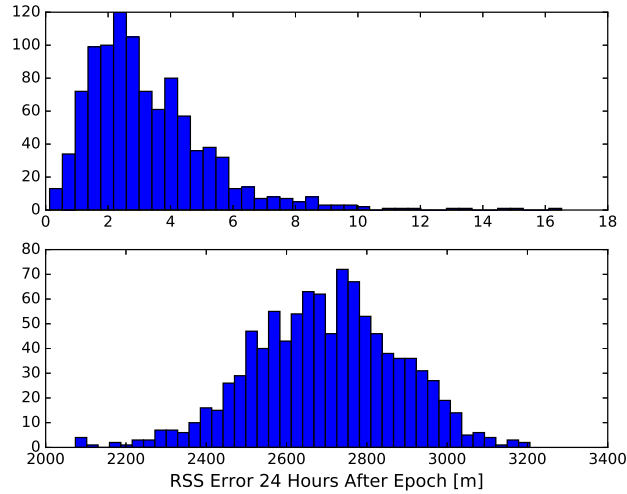


Figure 4: RSS error for high-fidelity corrected stochastic collocation (top) and uncorrected low-fidelity samples (bottom) for test case 1.

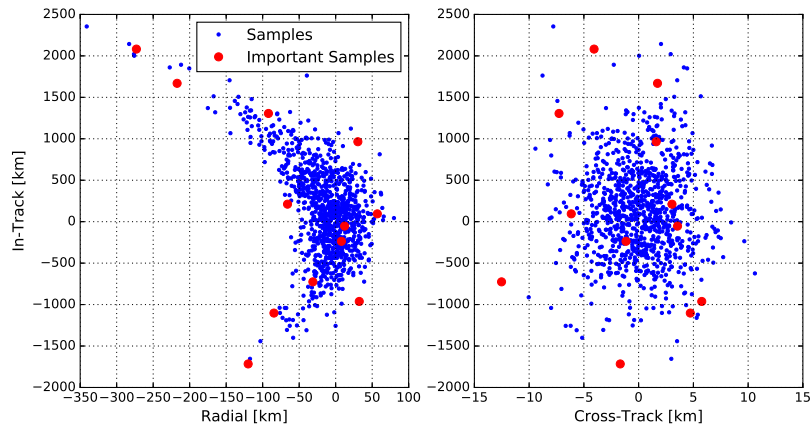


Figure 5: Scatter of propagated samples in the RIC frame of the propagated initial mean vector for test case 2.

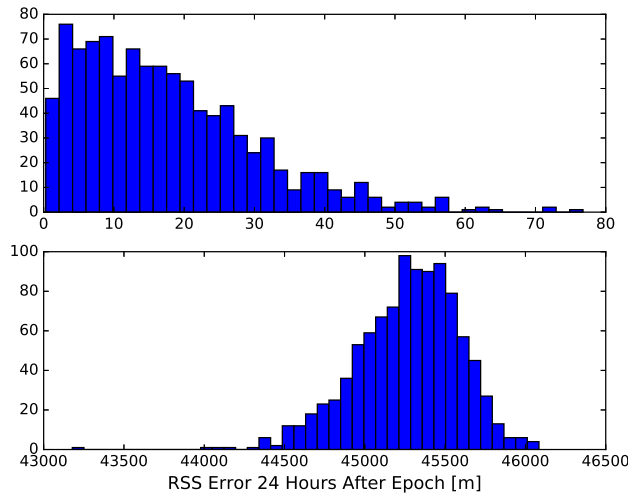


Figure 6: RSS error for high-fidelity corrected stochastic collocation (top) and uncorrected low-fidelity samples (bottom) for test case 2.

low-fidelity samples.

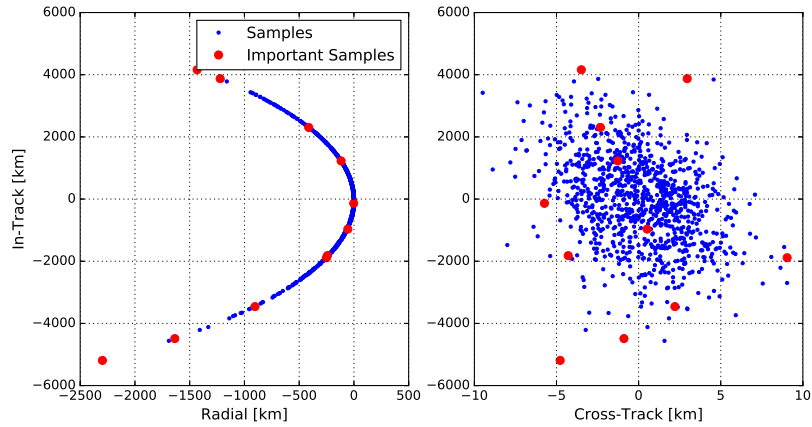


Figure 7: Scatter of propagated samples in the RIC frame of the propagated initial mean vector for test case 3.

Figure 7 demonstrates that the third case also produces a non-Gaussian

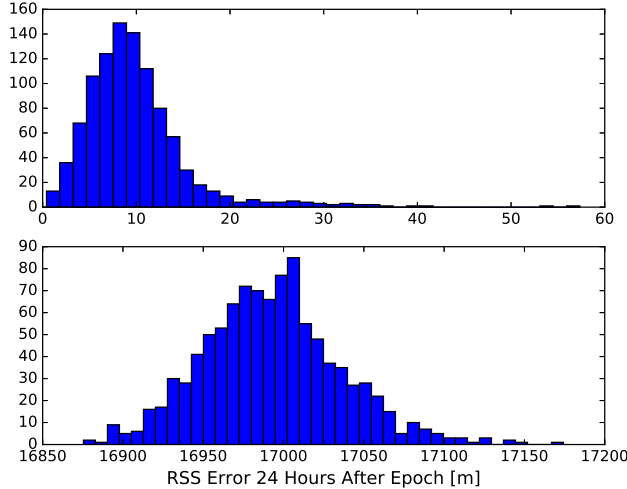


Figure 8: RSS error for high-fidelity corrected stochastic collocation (top) and uncorrected low-fidelity samples (bottom) for test case 3.

PDF at  $t_1 = 24$  hours after the epoch. The dispersion of the samples is similar to test case 1. With  $r = 11$ , Fig. 8 illustrates the distribution of RSS error for the corrected samples using the low-rank approximation. The error for most points is approximately 10 m with a maximum error of approximately 54 m.

Table 4: RMS error for low-fidelity and corrected samples

Test Case	$r$	$\mathbf{x}^L$ Error [km]	$\hat{\mathbf{x}}^H$ Error [km]
1	11	2.7029	0.0038
2	12	45.2675	0.0218
3	11	16.9928	0.0114

Table 4 summarizes the performance of the surrogate for the three test cases considered. RMS error of the low-fidelity propagated samples is on the order of kilometers due to force-model truncation, while the corrected samples  $\hat{\mathbf{x}}^H(\xi)$  achieve accuracies on the order of meters. While the highly-eccentric orbit demonstrates the largest RMS error in the corrected samples, it achieves the largest improvement relative to the  $\mathbf{x}^L(\xi)$  error. Errors are

reduced by employing a tri-fidelity model, which is described below.

*Table 5: Error in high-fidelity corrected samples as a function of low-fidelity model*

Force Model	RMS Error [m]		
	Test Case 1	Test Case 2	Test Case 3
Two-Body (TB) + $J_2$	3.8	21.8	11.4
TB + $10 \times 10$	1.3	10.1	7.5
TB + $J_2$ + Drag	4.0	11.6	10.3
TB + $J_2$ + SRP	3.9	17.4	17.8
TB + $J_2$ + Third Bodies	5.1	12.8	13.2
TB + $10 \times 10$ + Drag	0.8	7.4	2.5
TB + $20 \times 20$ + Drag	0.7	6.5	1.4
TB + $30 \times 30$ + Drag	0.3	8.0	0.7
TB + $40 \times 40$ + Drag	0.3	9.1	0.4
TB + $50 \times 50$ + Drag	0.5	5.5	0.3
TB + $60 \times 60$ + Drag	0.4	8.0	0.3
TB + $70 \times 70$ + Drag	0.3	5.6	0.4

Table 5 describes the effects of the selected low-fidelity model on the surrogate accuracy. Using a simple two-body with  $J_2$  perturbation yields surrogate accuracies on the order of 10s of meters or better. The second case exhibits a larger error than the other two, but, as illustrated later, propagation error when using the specified low-fidelity model is larger before correction. For all cases, including gravity perturbations and drag exhibit the largest improvement in surrogate accuracy, which is expected from knowledge of perturbation forces over the timespan examined.

*Table 6: Summary of execution times (seconds)*

Test Case	Surrogate Generation	$\widehat{\mathbf{X}}^H$	$\mathbf{X}^H$
1	7.02	1.51	378.67
2	2.97	0.55	71.35
3	7.07	1.47	447.92

Table 6 compares the execution times to propagate 1,000 samples via the stochastic collocation surrogate. The surrogate generation column quantifies

the time to propagate the 1,000 low-fidelity samples, select  $r$ , and execute the high-fidelity propagator using the important samples. The column denoted by  $\widehat{\mathbf{X}}^H$  describes the time to generate corrected samples for a new 1,000 points (includes the low-fidelity propagation of the new samples and applying the correction using the surrogate). The final column describes the time to propagate all 1,000 samples using the high-fidelity propagator. The average computation time of a high-fidelity propagation (third column divided by the number of samples) implies that approximately half of the surrogate generation time is spent propagating the 11-12 important samples.

*Table 7: Error in high-fidelity corrected samples as a function of medium-fidelity model*

Force Model	RMS Error [m]		
	Test Case 1	Test Case 2	Test Case 3
Two-Body (TB) + $J_2$	3.8	21.8	11.4
TB + $10 \times 10$	1.2	16.9	9.7
TB + $J_2$ + Drag	4.8	7.3	9.6
TB + $J_2$ + SRP	5.1	13.9	11.8
TB + $J_2$ + Third Bodies	5.4	13.0	11.7
TB + $10 \times 10$ + Drag	0.9	4.3	2.1
TB + $20 \times 20$ + Drag	0.4	4.3	1.5
TB + $30 \times 30$ + Drag	0.2	4.2	0.6
TB + $40 \times 40$ + Drag	0.3	3.9	0.4
TB + $50 \times 50$ + Drag	0.2	3.9	0.4
TB + $60 \times 60$ + Drag	0.2	4.0	0.3
TB + $70 \times 70$ + Drag	0.2	3.9	0.4
All	0.1	0.3	0.2

Table 7 demonstrates variations in performance when using a tri-fidelity propagation of the samples. This includes a comparison of RMS error as a function of the medium-fidelity force model with the bi-fidelity results from Table 4 included in the first row for reference. For these cases, RMS errors may be reduced by at least a factor of two by adding a medium-fidelity propagator. The GM model propagation results of the next section only use the bi-fidelity approach for the sake of simplicity.

### 5.1.2. Propagation of Gaussian Mixture Models

This section demonstrates the use of the multi-fidelity approach to reduce propagation time for a GM representation of the predicted PDF. This approach uses the same scenarios employed in the previous section with the two-body with  $J_2$  perturbation for low-fidelity propagation. To improve tractability in the baseline methods (see description below), this section uses *a priori* standard deviation values scaled by 0.1 for the state PDF. Results consider the case of  $D = 1, 2$ , or  $3$ , and also vary the number of components per direction. The PDF at epoch is split as described in Section 4.1, and the mixture is propagated via the approach in Section 4.4. Results are compared to an existing approach for propagating a GM approximation of the state PDF.

In [1], the authors propose a method to autonomously split GM components as part of the PDF prediction. This approach compares the entropy of a GM component propagated via linearization to the result using the unscented transform. This identifies when nonlinearity in the dynamics influence the single-component prediction. When the difference is above a given threshold, the component is split. In this case, we split a given component into three sub-components. This process continues until the propagator reaches the final time for all components. The authors dubbed this approach Adaptive Entropy-based Gaussian-mixture Information Synthesis (AEGIS). The implementation of AEGIS used here is only in C/C++ and uses the same propagation software as the multi-fidelity approach.

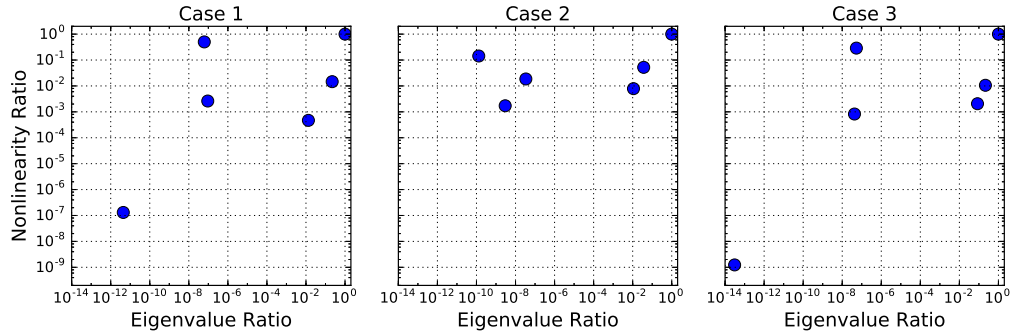


Figure 9: Nonlinearity and eigenvalue ratios for each test case and each component direction of the *a priori* covariance matrix.

Figure 9 illustrates the relative sensitivity of the posterior PDF at  $t_1$  to each of the eigendirections at  $t_0$  and the corresponding eigenvalues for all test

cases. These values are depicted as ratios (value divided by maximum value) to aid in visualizing their order. For each of these test cases, the relative magnitude of the eigenvalue does not correlate to its rank based on the nonlinearity measure  $NL(\hat{\mathbf{a}})$ . In Case 2, the smallest eigenvalue corresponds to the direction with the second largest nonlinearity ratio. As discussed in Section 4.2, some previous methods for GM propagation rank eigendirections for splitting by their corresponding eigenvalues. Figure 9 indicates that the ranking of eigenvalues does not always equal the ranking based on solution sensitivity. The nonlinearity ratio (24) is a direct measure of sensitivity at  $t_f$  to directions at  $t_0$ , and, hence, is used for ordering splitting directions in the multi-fidelity approach to propagating a GM.

To assess deviation from the true PDF estimated via Monte Carlo, we quantify accuracy using the likelihood agreement

$$L = \sum_{k=1}^K \sum_{j=1}^J \gamma_k w_j p_N \left( \begin{bmatrix} \mathbf{r}(t_1, \xi_k) \\ \dot{\mathbf{r}}(t_1, \xi_k) \end{bmatrix}; \mathbf{m}_j, \mathbf{P}_j \right), \quad (29)$$

where  $\mathbf{r}(t_1, \xi_k)$  and  $\dot{\mathbf{r}}(t_1, \xi_k)$  are the propagated Monte Carlo position and velocity, respectively, each with equal weight  $\gamma_k = 1/K$ . The same approach was leveraged in [1] to demonstrate the improved PDF accuracy when compared to a single Gaussian component. Likelihood agreement for the AEGIS-propagated PDFs is also included.

Figure 10 presents the resulting accuracy (measured by  $L$ ) for each test case as a function of the GM splitting design parameters. Results include variations in the number of splitting directions and the number of components in each direction. In all cases, increasing the number of directions for the GM split at  $t_0$  improves results. However, results indicate a diminishing return since improvements reduce when moving from two to three directions. For the low-altitude cases, the baseline method requires more components to achieve a comparable value of  $L$ . For the second case, the  $D = 2$  and AEGIS methods exhibit similar PDF agreement with the Monte Carlo solution.

Figure 11 illustrates the runtime required to generate the propagated GM via the multi-fidelity approach. The indicated runtime includes the splitting of the priori PDF at  $t_0$ , the generation of the propagated sigma points via the multi-fidelity approach, and solving for the mean and covariance via the unscented transform for the  $J$  components. Propagation of the sigma points via the low-fidelity model leverages parallelization over six cores using the IPyParallel module in Python. While not included in the plot, approximately

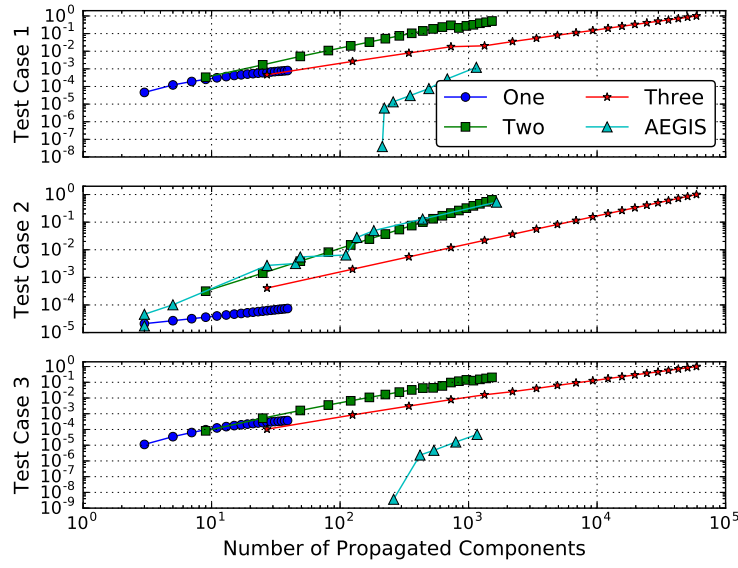


Figure 10: Ratio of likelihood values ( $L/L_{\max}$ ) for each test case and a given number of splitting directions (one through three) as a function of  $J$ .

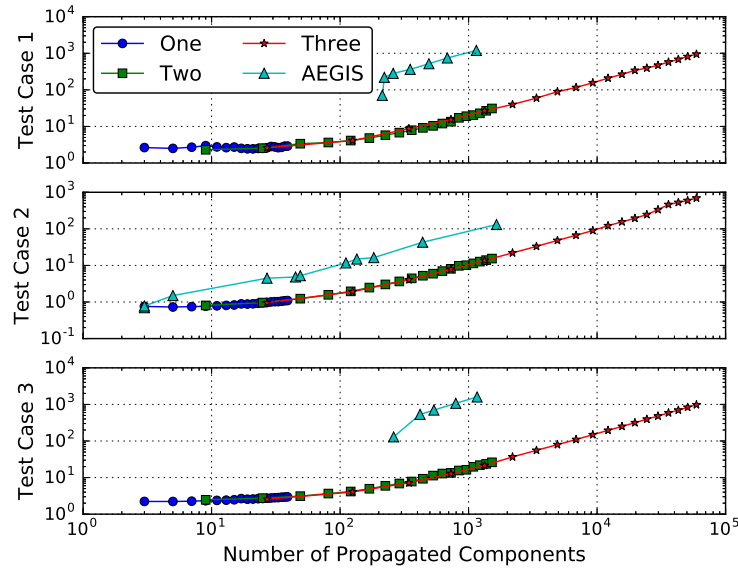


Figure 11: Runtime (in seconds) to generate the GM approximation as a function of  $J$ .

half of the runtime is spent on the GM component splitting and generation of the mean and covariance using the propagated sigma points. Further runtime reduction may be achieved through parallelization of such operations and converting the Python portions of the software to C/C++. Results indicate runtime is determined by the number of components independent of the number of splitting directions, which is expected. In all cases, AEGIS requires a longer runtime. Profiling the software demonstrates that 99.9% of the runtime for AEGIS is spent in evaluating the high-fidelity force models.

The combination of Figs 10 and 11 indicates that, for these test cases, leveraging a GM split in two directions yields sufficient accuracy without the increased computation cost of an additional direction. A two-dimension split and the multi-fidelity approach also yield improved accuracy ( $L$ ) performance and greatly reduces runtime when compared to the AEGIS method. Running AEGIS for the standard deviation values in Table 1 proved to be prohibitive due to runtime requirements.

### 5.2. Two-Line Element Set Case

This section describes bi-fidelity propagation of uncertainty where the mean of the *a priori* PDF is based on a TLE for the GRACE-1 satellite. This satellite is in a nearly circular, 500 km altitude orbit with an inclination of approximately 89°. The low-fidelity propagator is the Simplified General Perturbations 4 (SGP4) propagator (e.g., see [31]), which is standard for propagating TLEs, but only includes averaged effects for central body,  $J_2-J_4$ , and atmospheric drag (with spherical, exponential density) in the True Equator, Mean Equinox (TEME) frame for low-Earth orbiting satellites (orbit period less than 225 minutes). Tables 8 and 9 describe the force models and parameters, respectively, for the high-fidelity model. Truth is defined as the orbit determination ephemeris with a precision on the order of centimeters [32]. The TLE is provided for reference in Figure 12, and tests consider propagation of uncertainty over various durations. Table 10 describes the standard deviations of the PDF in the TEME Cartesian RIC frame, which are selected to bound the TLE approximation error at epoch when compared to the precise GRACE-1 ephemeris. These are converted to a Gaussian PDF in the orbital elements in the TEME frame using the unscented transform.

Figures 13-15 describe the corrected and uncorrected samples for propagation times of 1.73, 7.32, and 30.37 days, respectively. The precise ephemeris defines the origin and basis vectors for the RIC frame, and the positions in the figures indicate location relative to the ground truth. The longer-duration

Table 8: High-fidelity force models for SGP4 tests

Model	High-Fidelity
Central Body Gravity	$200 \times 200$ with solid tides
Third-Body Perturbations	Sun, Moon, and Jupiter
Solar Radiation Pressure	Cannonball
Atmospheric Drag	Cannonball
Earth Radiation Pressure	Cannonball [33]
Coordinate System Reduction	IAU2006 [30]

Table 9: Force model and satellite parameters for SGP4 cases

Parameter	Value
Drag $A/m$	$2 \times 10^{-3} \text{ m}^2/\text{kg}$
SRP $A/m$	$4 \times 10^{-3} \text{ m}^2/\text{kg}$
$C_D$	2.0
$C_R$	1.8

1	27391U	02012A	04001.41972880	.00003076	00000-0	10551-3	0	9992
2	27391	089.0141	267.6901	0015065	280.5137	079.4371	15.29725983	99955

Figure 12: TLE at epoch for the GRACE-1 satellite

Table 10: A priori PDF standard deviations in RIC coordinates for TLE case

Component	<b>R</b>	<b>I</b>	<b>C</b>
Position [km]	0.02	1.2	0.1
Velocity [ $\times 10^{-4}$ km/s]	20	0.2	0.3

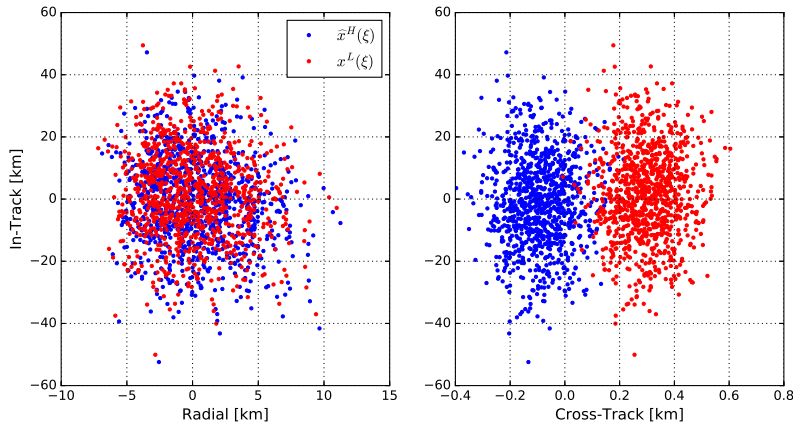


Figure 13: Low-fidelity and corrected high-fidelity samples propagated for 1.37 days for the SGP4 case. The RIC frame is defined by the GRACE-1 precise ephemeris.

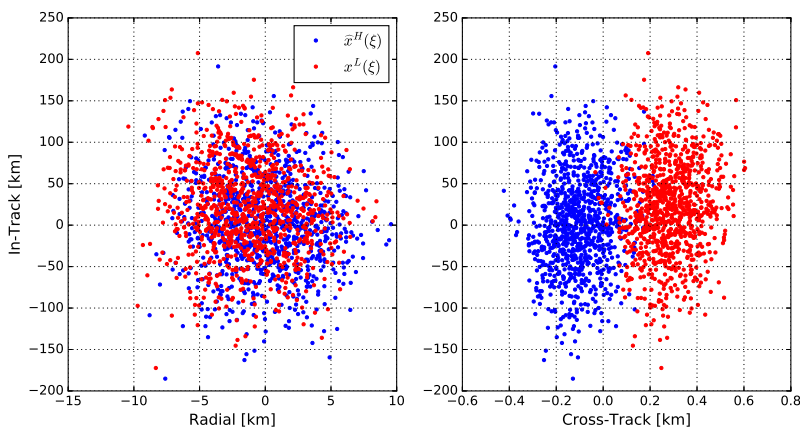
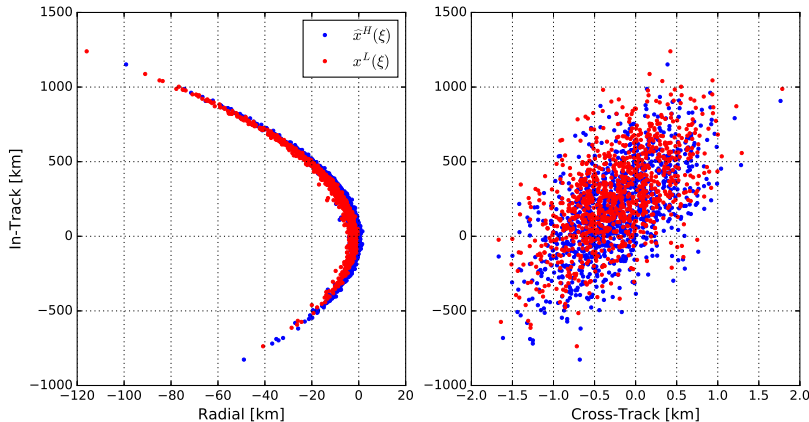


Figure 14: Low-fidelity and corrected high-fidelity samples propagated for 7.32 days for the SGP4 case. The RIC frame is defined by the GRACE-1 precise ephemeris.



*Figure 15: Low-fidelity and corrected high-fidelity samples propagated for 30.37 days for the SGP4 case. The RIC frame is defined by the GRACE-1 precise ephemeris.*

propagations yield a larger correction in the in-track direction, which corresponds to the error in the propagated mean. In all cases, the corrected solution yields improved consistency with the truth defined by the precise ephemeris. This illustrates the potential improvement that may be achieved when augmenting samples propagated via SGP4 with a stochastic collocation surrogate that includes a high-fidelity correction.

## 6. Conclusions

This paper demonstrates reduced computation time when employing a multi-fidelity approach to orbit state uncertainty propagation. This includes propagation of the state PDF represented as a particle ensemble or a Gaussian mixture model. The developed method requires propagating desired samples to the time or times of interest using a low-fidelity propagator, and applies a data-derived correction using a small number of high-fidelity propagations. These corrections yield root-mean-square errors on the order of meters to 10s of meters over the complete sample set. The approach also demonstrates the ability to correct samples propagated used general perturbation theory, i.e., SGP4, with a small number of high-fidelity samples using special perturbation models. Several future applications of this work exist, including, but not limited to, adaptive propagation of GM models and

implementation in orbit determination filters for astrodynamics applications.

## 7. Acknowledgements

This work was funded by the Air Force Research Laboratory Summer Faculty Fellowship (AFRL-SFFP) program. The authors thank Alireza Doostan of the University of Colorado Boulder for his helpful discussions on his work in [18]. Vivek Vittaldev, formerly of The University of Texas at Austin, provided the splitting library used for the GM model results. We also thank Kyle DeMars of the Missouri University of Science and Technology for his discussions on AEGIS.

## 8. Appendix

Algorithm 1 summarizes how to generate  $\mathbf{L}$  and the list of indices  $\mathcal{I}$  used to get  $\bar{\Xi}^r$ . Note that  $L_{i,j}$  refers to the element in the  $i$ th row and  $j$ th column of  $\mathbf{L}$ , and  $\mathbf{V}_{:,i}$  refers to the  $i$ th column of  $\mathbf{V}$ . While not immediately addressed in the algorithm, some bookkeeping is required when using the output list of indices  $\mathcal{I}$  since the column swapping changes the order of columns in  $\mathbf{V}$ , i.e.,  $\mathbf{V} \neq \mathbf{X}^L$  after algorithm completion. The stopping condition compares a weight to some lower tolerance  $\epsilon$ , e.g., machine precision, to prevent an ill-conditioned  $\mathbf{L}$ .

**Data:**  $\mathbf{X}^L$  and  $r$

**Result:** ordered list of indices  $\mathcal{I}$  corresponding to important samples and decomposition  $\mathbf{L}$

```

 $\mathbf{V} = \mathbf{X}^L;$ 
 $w_\ell = \mathbf{V}_{:, \ell}^T \mathbf{V}_{:, \ell}$  for  $\ell = 1, \dots, m$ ;
 $\mathcal{I} = \emptyset$ ,  $\mathbf{L} = \mathbf{0} \in \mathbb{R}^{m \times r}$ ;
for  $n = 1, \dots, r$  do
     $e, i = \arg \max_{\ell \in \{n, \dots, m\}} w_\ell$ ;
    if  $e < \epsilon$  then
         $n = n - 1$ ;
        stop
    end
     $\mathcal{I} = \mathcal{I} \cup \{i\}$ ;
    Swap the  $n$ th and  $i$ th columns in  $\mathbf{V}$ ;
    Swap the values of  $w_i$  and  $w_n$ ;
     $v_t = \mathbf{V}_{:, t}^T \mathbf{V}_{:, n} - \sum_{j=1}^{N-1} L_{t,j} L_{n,j}$ , for  $t = n + 1, \dots, m$ ;
     $L_{n,n} = \sqrt{w_n}$ ;
     $L_{t,n} = v_t / L_{n,n}$ , for  $t = n + 1, \dots, m$ ;
     $w_t = w_t - L_{t,n}^2$ , for  $t = n + 1, \dots, m$ ;
end
 $\mathbf{L} = \mathbf{L}(1:n, 1:n)$ ;

```

**Algorithm 1:** Identification of  $r$  most important samples.

## References

- [1] K. J. DeMars, R. H. Bishop, M. K. Jah, Entropy-based approach for uncertainty propagation of nonlinear dynamical systems, *Journal of Guidance, Control, and Dynamics* 36 (4) (2013) 1047–1057. doi:10.2514/1.58987.
- [2] J. T. Horwood, A. B. Poore, Adaptive gaussian sum filters for space surveillance, *IEEE Transactions on Automatic Control* 56 (8) (2011) 1777–1790. doi:10.2514/1.53793.
- [3] B. A. Jones, A. Doostan, G. H. Born, Nonlinear propagation of orbit uncertainty using non-intrusive polynomial chaos, *Journal of Guidance, Control, and Dynamics* 36 (2) (2013) 430–444. doi:10.2514/1.57599.
- [4] B. A. Jones, A. Doostan, Satellite collision probability estimation using polynomial chaos expansions, *Advances in Space Research* 52 (11) (2013) 1860–1875. doi:10.1016/j.asr.2013.08.027.
- [5] B. A. Jones, N. Parrish, A. Doostan, Postmaneuver collision probability estimation using sparse polynomial chaos expansions, *Journal of Guidance, Control, and Dynamics* 38 (8) (2015) 1425–1437. doi:10.2514/1.G000595.
- [6] R. S. Park, D. J. Scheeres, Nonlinear mapping of Gaussian statistics: Theory and applications to spacecraft trajectory design, *Journal of Guidance, Control, and Dynamics* 29 (6) (2006) 1367–1375.
- [7] K. Fujimoto, D. J. Scheeres, K. T. Alfriend, Analytical nonlinear propagation of uncertainty in the two-body problem, *Journal of Guidance, Control, and Dynamics* 35 (2) (2012) 497–509. doi:10.2514/1.54385.
- [8] M. Majji, J. L. Junkins, J. D. Turner, A high order method for estimation of dynamic systems, *Journal of the Astronautical Sciences* 56 (3).
- [9] R. Armellin, P. Di Lizia, F. Bernelli-Zazzera, M. Berz, Asteroid close encounters characterization using differential algebra: the case of Apophis, *Celestial Mechanics and Dynamical Astronomy* 107 (4) (2010) 451–470.
- [10] M. Valli, R. Armellin, P. Di Lizia, M. R. Lavagna, Nonlinear mapping of uncertainties in celestial mechanics, *Journal of Guidance, Control, and Dynamics* 36 (1) (2013) 48–63. doi:10.2514/1.58068.

- [11] N. Arora, R. P. Russell, Efficient interpolation of high-fidelity geopotentials, *Journal of Guidance, Control, and Dynamics* 39 (1) (2016) 128–143. doi:10.2514/1.G001291.
- [12] B. A. Jones, G. H. Born, G. Beylkin, Comparisons of the cubed-sphere gravity model with the spherical harmonics, *Journal of Guidance, Control, and Dynamics* 33 (2) (2010) 415–425.
- [13] A. Awad, A. Narang-Siddarth, R. Weisman, Method of multiple scales for orbit propagation with nonconservative forces, *Journal of Guidance, Control, and Dynamics* 40 (6) (2017) 1457–1465. doi:10.2514/1.G002287.
- [14] B. K. Bradley, B. A. Jones, G. Beylkin, K. Sandberg, P. Axelrad, Bandlimited implicit Runge-Kutta integration for astrodynamics, *Celestial Mechanics and Dynamical Astronomy* 119 (2) (2014) 143–168. doi:10.1007/s10569-014-9551-x.
- [15] B. Peherstorfer, K. Willcox, M. Gunzburger, Survey of multifidelity methods in uncertainty propagation, inference, and optimization, To appear in *SIAM Review*, Technical Report TR-16-1, Aerospace Computational Design Laboratory, Massachusetts Institute of Technology (2016).
- [16] A. Narayan, C. Gittelson, D. Xiu, A stochastic collocation algorithm with multifidelity models, *SIAM Journal on Scientific Computing* 36 (2) (2014) A495–A521. doi:10.1137/130929461.
- [17] X. Zhu, A. Narayan, D. Xiu, Computational aspects of stochastic collocation with multifidelity models, *SIAM/ASA Journal on Uncertainty Quantification* 2 (1) (2014) 444–463. doi:10.1137/130949154.
- [18] A. Doostan, , G. Geraci, G. Iaccarino, A bi-fidelity approach for uncertainty quantification of heat transfer in a rectangular ribbed channel, in: *Proceedings of ASME Turbo Expo 2016: Turbomachinery Technical Conference and Exposition*, Seoul, South Korea, 2016.
- [19] I. Park, D. J. Scheeres, Optimization of hybrid method for uncertainty propagation of non-keplerian motion, in: *AIAA/AAS Astrodynamics Specialist Conference*, AIAA 2016-5630, Long Beach, California, 2016. doi:doi:10.2514/6.2016-5630.

- [20] J.-N. Juang, Applied System Identification, Prentice-Hall PTR, Englewood Cliffs, New Jersey, 1994.
- [21] J. Hampton, H. Fairbanks, A. Narayan, A. Doostan, Parametric/stochastic model reduction: Low-rank representation, non-intrusive bi-fidelity approximation, and convergence analysis, Under review, preprint at <https://arxiv.org/abs/1709.03661>, 2017.
- [22] S. Gehly, B. A. Jones, P. Axelrad, Sensor allocation for tracking geosynchronous space objects, *Journal of Guidance, Control, and Dynamics* 41 (1) (2018) 149–163. doi:10.2514/1.G000421.
- [23] B. D. Tapley, B. E. Schutz, G. H. Born, Statistical Orbit Determination, 1st Edition, Elsevier Academic Press, Burlington, MA, 2004.
- [24] S. J. Julier, J. K. Uhlmann, A new extension of the Kalman filter to nonlinear systems, *Proceedings of SPIE* 3068 (1997) 182–193.
- [25] R. Van der Merwe, E. A. Wan, The square-root unscented Kalman filter for state and parameter-estimation, in: 2001 IEEE International Conference on Acoustics, Speech, and Signal Processing, Vol. 6, Salt Lake City, Utah, 2001, pp. 3461–3464.
- [26] H. Sorenson, D. Alspach, Recursive bayesian estimation using gaussian sums, *Automatica* 7 (4) (1971) 465 – 479. doi:10.1016/0005-1098(71)90097-5.
- [27] D. L. Alspach, H. W. Sorenson, Nonlinear Bayesian estimation using Gaussian sum approximations, *IEEE Transactions on Automatic Control* AC-17 (4) (1972) 439–448. doi:10.1109/TAC.1972.1100034.
- [28] V. Vittaldev, R. P. Russell, Multidirectional Gaussian mixture models for nonlinear uncertainty propagation, *Computer Modeling in Engineering and Sciences* 111 (1) (2016) 83–117. doi:10.3970/cmes.2016.111.083.
- [29] W. M. Folkner, J. G. Williams, D. H. Boggs, R. S. Park, P. Kuchynka, The planetary and lunar ephemerides DE430 DE431, IPN Progress Report 42-196, Jet Propulsion Laboratory, California Institute of Technology, [http://ipnpr.jpl.nasa.gov/progress\\_report/42-196/196C.pdf](http://ipnpr.jpl.nasa.gov/progress_report/42-196/196C.pdf) (February 2009).

- [30] G. Petit, B. Luzum, Iers conventions (2010), IERS Technical Note 36, International Earth Rotation and Reference Systems Service (IERS), Frankfurt am Main, Germany (2010).
- [31] D. A. Vallado, P. Crawford, R. Hujasak, T. S. Kelso, Revisiting space-track report #3, in: AIAA/AAS Astrodynamics Specialist Conference, Keystone, Colorado, 2006.
- [32] Z. Kang, B. Tapley, S. V. Bettadpur, J. C. Ries, P. Nagel, R. Pastor, Precise orbit determination for the GRACE mission using only GPS data, *Journal of Geodesy* 80 (6) (2006) 322–331.
- [33] P. C. Knocke, J. C. Ries, B. D. Tapley, Earth radiation pressure effects on satellites, in: AIAA/AAS Astrodynamics Specialist Conference, Minneapolis, Minnesota, 1988.

## Multi-Fidelity Orbit Uncertainty Propagation Paper Highlights

- Multi-fidelity approach reduces runtime for orbit-state uncertainty propagation.
- Combines low- and high-fidelity models for orbit state propagation.
- Apply a high-fidelity correction to low-fidelity samples via stochastic collocation
- Demonstrate with particle and Gaussian mixture approaches to uncertainty propagation.